A Theory of the Wind-Driven Beaufort Gyre Variability

GEORGY E. MANUCHARYAN

Division of Geological and Planetary Sciences, California Institute of Technology, Pasadena, California

MICHAEL A. SPALL

Department of Physical Oceanography, Woods Hole Oceanographic Institution, Woods Hole, Massachusetts

ANDREW F. THOMPSON

Division of Geological and Planetary Sciences, California Institute of Technology, Pasadena, California

(Manuscript received 11 April 2016, in final form 22 July 2016)

ABSTRACT

The halocline of the Beaufort Gyre varies significantly on interannual to decadal time scales, affecting the freshwater content (FWC) of the Arctic Ocean. This study explores the role of eddies in the Ekman-driven gyre variability. Following the transformed Eulerian-mean paradigm, the authors develop a theory that links the FWC variability to the stability of the large-scale gyre, defined as the inverse of its equilibration time. The theory, verified with eddy-resolving numerical simulations, demonstrates that the gyre stability is explicitly controlled by the mesoscale eddy diffusivity. An accurate representation of the halocline dynamics requires the eddy diffusivity of $300 \pm 200\,\mathrm{m^2\,s^{-1}}$, which is lower than what is used in most low-resolution climate models. In particular, on interannual and longer time scales the eddy fluxes and the Ekman pumping provide equally important contributions to the FWC variability. However, only large-scale Ekman pumping patterns can significantly alter the FWC, with spatially localized perturbations being an order of magnitude less efficient. Lastly, the authors introduce a novel FWC tendency diagnostic—the Gyre Index—that can be conveniently calculated using observations located only along the gyre boundaries. Its strong predictive capabilities, assessed in the eddy-resolving model forced by stochastic winds, suggest that the Gyre Index would be of use in interpreting FWC evolution in observations as well as in numerical models.

1. Introduction

The observed increase of the Arctic freshwater content over the past two decades has been related partially to a deepening of the halocline and partially to water mass freshening (Rabe et al. 2014). In particular, a significant contribution to the overall Arctic freshening came from the Beaufort Gyre; here, the freshwater content (FWC) increased by about 30% over the past decade (Haine et al. 2015).

Observational evidence suggests that the halocline dynamics of the Beaufort Gyre are to a large extent governed by the anticyclonic atmospheric winds that drive the large-scale gyre circulation—and to a lesser extent due to the availability of Arctic freshwater sources (Proshutinsky et al. 2009). The surface stress results largely from the sea ice drag and quantification of the oceanic response is subject to our uncertainties in the sea ice–ocean momentum exchange (Martin et al. 2014; Giles et al. 2012).

Modeling and observational studies demonstrate a direct relation between the freshwater content and the Ekman pumping (Proshutinsky et al. 2002, 2009; Stewart and Haine 2013; Timmermans et al. 2011, 2014). Thus, Stewart and Haine (2013) show that a reduction in the

Corresponding author address: Georgy E. Manucharyan, MC 131-24, California Institute of Technology, 1200 East California Boulevard, Pasadena, CA 91125.
E-mail: gmanuch@caltech.edu

DOI: 10.1175/JPO-D-16-0091.1

strength of anticyclonic winds can lead to a redistribution of FWC within the Arctic Ocean and to changes in the exchange between the North Atlantic and Pacific Oceans. The basic gyre dynamics are conventionally described in the following way: the surface Ekman transport converges surface fresh waters and deepens the halocline, thus storing freshwater in the gyre (e.g., Proshutinsky et al. 2009). This argument, however, does not explain how a steady state can be achieved, as it does not specify a mechanism opposing the continuous halocline deepening due to the Ekman pumping.

The importance of the opposing mechanism can be clearly illustrated from the point of view of the large-scale gyre stability in its integral sense. By stability, we imply that there exists a statistical equilibrium state of the gyre (averaged over small-scale features; e.g., internal waves and eddies) and that any deviations from this equilibrium would decay on a finite time scale. Since the gyre is a persistent, large-scale feature of the Arctic Ocean, it is reasonable to assume that it is a stable, externally driven system. Using basic concepts of dynamical systems theory (e.g., Tabor 1989), the linear stability assumption implies that near its equilibrium, perturbations of the gyre state a obey a basic equation of forced exponential decay:

$$\frac{da}{dt} = -\frac{a}{T} + w. \tag{1}$$

We will formally derive Eq. (1) in this manuscript (see section 6), providing physical interpretation for its variables, but at this point one can conceptually think of a and w as measures of the bulk halocline deepening (or FWC) and Ekman pumping correspondingly. The gyre stability is defined as the inverse of its equilibration time scale T, and here we assume that the large-scale gyre circulation is always stable (i.e., $T > 0$). The damping term $(-a/T)$ represents a linearization of a process opposing the Ekman pumping near its equilibrium.

Here, it is important to distinguish the concepts of large-scale gyre stability in terms of a statistically averaged equilibrium, and this state's hydrodynamic stability characteristics. By gyre stability, we refer to the equilibration (exponential decay) of large-scale anomalies of a statistically averaged circulation that does not contain information about individual small-scale eddies. In contrast, baroclinic instabilities lead to the exponential growth of individual small-scale perturbations. Thus, the gyre can be stable in a statistically averaged sense and at the same time hydrodynamically unstable at small scales. Our proposed hypothesis implies that the stability of the large-scale gyre depends on the cumulative action of small-scale eddies, individually generated through baroclinic instabilities.

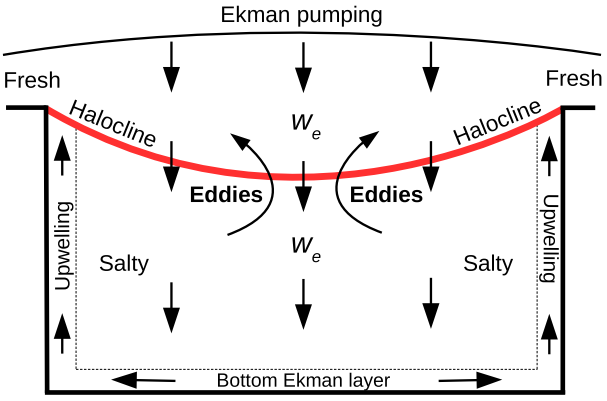

FIG. 1. Schematic view of the Beaufort Gyre circulation depicting a balance between Ekman pumping and eddy-induced vertical velocity. The Ekman vertical velocity penetrates through the entire water column. Surface convergence of the Ekman transport is balanced by the corresponding bottom divergence with the mean circulation being closed via coastal upwelling.

Based on a basic, dimensional analysis, the halocline deepening (units of meters) should depend not only on Ekman pumping (units of meters per second) but also on the adjustment time scale (units of seconds). For example, according to Eq. (1), $a = wT$ for a system in steady state or subject to a slowly evolving forcing. Moreover, the amplitude of the gyre variability in response to time-dependent Ekman pumping would also be directly proportional to T (i.e., reduced stability would imply a larger variance for the same forcing). Since the gyre stability is directly related to the nature of the processes that counteract the Ekman pumping, it is essential to determine what these processes are, how they depend on external forcing, and how they affect the gyre variability.

While much of the scientific effort has been devoted to the exploration of the impact of Ekman pumping (e.g., Proshutinsky et al. 2002; Yang 2009; McPhee 2012; Timmermans et al. 2014; Cole et al. 2014), factors controlling the gyre stability are poorly understood. A recently proposed hypothesis points to mesoscale eddy transport being a sufficient mechanism to oppose the Ekman pumping (Davis et al. 2014; Marshall 2015; Lique et al. 2015; Manucharyan and Spall 2016, hereinafter MS16; Yang et al. 2016). The eddies are generated via baroclinic instabilities of the large-scale gyre circulation that releases available potential energy associated with the halocline deepening. The eddy buoyancy fluxes (or layer thickness fluxes) throughout this process act to adiabatically flatten the halocline, thus opposing the deepening due to the Ekman pumping (schematically shown in Fig. 1).

The mesoscale eddies discussed here are associated with baroclinic instabilities of a large-scale halocline slope and hence predominantly carry the energy of the first baroclinic mode. The majority of the observational analysis in the Arctic Ocean, however, has been devoted to intense, localized vortices (Manley and Hunkins 1985; Timmermans et al. 2008; Dmitrenko et al. 2008; Watanabe 2011; Zhao et al. 2014) that can form at boundary currents (Watanabe 2013; Spall et al. 2008; Spall 2013) and at surface ocean fronts (Manucharyan and Timmermans 2013). Although observational analysis for the role of halocline-origin eddies in the interior salinity budget is currently lacking, this is likely due to a lack of data sufficient to calculate energy conversion rates and eddy salt fluxes in the basin interior.

Taking into account the eddy transport mechanism, Davis et al. (2014) have used a low-resolution, shallow-water model (with eddies parameterized as horizontal diffusion) to explore seasonal gyre dynamics. Yang et al. (2016) explored the potential vorticity budget of the gyre and reached the conclusion that eddies are necessary to close it. Previous studies have suggested that there are links between the dynamics governing the Antarctic Circumpolar Current (ACC; Marshall and Radko 2003) and gyres with azimuthally symmetric circulations: Su et al. (2014) in the Weddell Gyre, Marshall et al. (2002) in laboratory experiments, and Marshall (2015) in the Beaufort Gyre. The stratification in these regions is determined from a leading-order balance between mesoscale eddy transport and Ekman pumping.

A recent study by MS16 demonstrated that the instabilities associated with the observed halocline slope are indeed generating sufficient mesoscale activity to cumulatively counteract the Ekman pumping. They also developed a set of analytical scaling laws that predict the gyre adjustment time scale, halocline depth, and maximum freshwater flux out of the gyre and explicitly relate these key gyre characteristics to the mesoscale eddy dynamics.

In light of this newly developed understanding, it is imperative to explore the role of mesoscale eddies in determining the stability of the gyre and its transient dynamics. Here, we present a basic theory of the wind-driven Beaufort Gyre variability. The manuscript is organized in the following way: In section 2, we briefly review the transformed Eulerian-mean framework that is used throughout our analysis. In section 3, we describe an idealized Beaufort Gyre model that we use for our process studies. In section 4, we diagnose a key eddy field characteristic, the eddy diffusivity, and assess its sensitivity to forcing. In section 5, we demonstrate how mesoscale eddies affect the gyre stability and equilibration. In section 6, we quantify the FWC response to periodic and spatially inhomogeneous Ekman pumping. In section 7, we introduce a new Gyre Index (GI) that includes the effects of both Ekman pumping and mesoscale eddies in order to rationalize FWC variability. We summarize and discuss implications in section 8.

2. Theoretical background

We briefly describe the mathematical formulation of the transformed Eulerian-mean framework (TEM; Andrews and McIntyre 1976; Vallis 2006; Marshall and Radko 2003) that is used in our analysis. Within this framework the eddy buoyancy fluxes can be represented via an additional eddy-induced streamfunction. This allows one to view the ensemble-mean buoyancy as being advected by the residual between the Eulerian mean and the eddy-driven circulations.

a. TEM framework

The Reynolds averaged buoyancy equation is written in cylindrical coordinates as

$$\overline{b}_t + \overline{v}\overline{b}_r + \overline{w}\overline{b}_z + \overline{(v'b'_r)} + \overline{(w'b'_z)} = \overline{S}, \tag{2}$$

where b denotes the buoyancy, $(\overline{v}, \overline{w})$ are the Eulerian-mean radial and vertical velocities in the (r, z) coordinates, and S represents buoyancy sources and sinks. The bar here represents an average either in the azimuthal direction or in an ensemble-mean sense; we only consider axisymmetric solutions here. Next, the eddy buoyancy fluxes are assumed to be predominantly aligned with isopycnals in the interior of the ocean—the so-called adiabatic limit (Vallis 2006). In this limit the flux divergences can be represented as an additional advection of mean gradients by the eddy streamfunction such that

$$\overline{b}_t + (\overline{v} + v^*)\overline{b}_r + (\overline{w} + w^*)\overline{b}_z = \overline{S}, \tag{3}$$

where the eddy advection velocities can be defined from an eddy streamfunction ψ^* as

$$\psi^* = -\frac{\overline{w'b'}}{\overline{b}_r} = \frac{\overline{v'b'}}{\overline{b}_z}, \quad \text{and} \tag{4}$$

$$u^* = -\psi^*_z, \quad w^* = \frac{1}{r}(r\psi^*)_r. \tag{5}$$

The adiabatic assumption breaks down near boundary layers that have significant diabatic fluxes due to buoyancy forcing and/or enhanced mixing. Near such boundaries the processes obey different dynamics that we do not attempt to represent here.

Thus, the ensemble-mean buoyancy is advected by a residual circulation $\tilde{\psi} \equiv \overline{\psi} + \psi^*$ that exists in order to balance the buoyancy sources and sinks. This formalism

clarifies that in the interior of the ocean, where the diabatic fluxes are small, a steady state implies that the residual circulation has to vanish, that is, $\tilde{\psi} = 0$.

At this point, in order to make analytical progress in understanding the buoyancy variability, it is necessary to introduce a closure for the eddy-driven streamfunction and to determine the Eulerian-mean streamfunction.

b. *Eulerian-mean streamfunction*

The azimuthally averaged azimuthal momentum equation can be simplified for the gyre dynamics. First, we assume that contributions from the Reynolds stresses are negligible for large-scale flows. Second, the inertial term can also be neglected for time scales sufficiently larger than f^{-1}, where f is the Coriolis parameter. In addition, the azimuthal pressure gradient term vanishes as a result of azimuthal averaging. Taking this into account, a simplified form of the momentum equation represents the steady Ekman dynamics:

$$f\overline{v} = -\overline{\tau}_z/\rho_0, \tag{6}$$

where τ is the azimuthal stress and $\rho_0 = 1023\,\mathrm{kg\,m^{-3}}$ is the reference ocean density. In the ocean interior, the vertical shear in stress is negligible, allowing one to obtain an expression for the Eulerian streamfunction by vertically integrating the momentum equation from the surface to any depth below the surface Ekman layer:

$$\overline{\psi} = \frac{\tau}{\rho_0 f}, \quad \text{and} \tag{7}$$

$$\overline{v} = -\overline{\psi}_z, \quad \overline{w} = \frac{1}{r}(r\overline{\psi})_r. \tag{8}$$

From now on $\tau = \tau(r, t)$ denotes the radially and time-dependent azimuthal surface stress—an external forcing for the gyre. Thus, the large-scale, Eulerian-mean flow is entirely determined by the surface stress distribution and does not depend on the buoyancy field or the mesoscale eddy activity. Note that this relation can be significantly affected by the presence of topography.

c. *Mesoscale eddy parameterization*

Mesoscale eddies emerge due to an instability of the baroclinic flow and their amplitude is related to the stability characteristics of the flow. Here, we implement a Gent–McWilliams type mesoscale eddy parameterization (Gent and Mcwilliams 1990) that assumes a downgradient nature for the eddy buoyancy fluxes (or layer thickness fluxes):

$$\overline{v'b'} = -K\overline{b}_r. \tag{9}$$

The eddy diffusivity $K = K(s)$ can in general depend on the magnitude of the isopycnal slope $s = |\overline{b}_r/\overline{b}_z|$, thus varying in space and time. Past studies suggested power-law dependencies ($K \sim s^{n-1}$). Powers $n = 1$ or $n = 2$ (Gent and Mcwilliams 1990; Visbeck et al. 1997) are commonly used in low-resolution ocean models, while MS16 suggest that $n = 3$ might be more appropriate for the Beaufort Gyre. Since observations are not sufficient to differentiate between these parameterizations, we continue the analysis assuming a general power-law dependence:

$$\psi^* = K\overline{s} = k\overline{s}^n, \tag{10}$$

where now k (having units of meters squared per second) is a constant that we will refer to as eddy efficiency to distinguish it from time- and space-dependent eddy diffusivity K.

d. *Steady state*

In the absence of surface buoyancy forcing or strong vertical mixing, the steady-state residual ocean circulation has to vanish (Marshall and Radko 2003; Su et al. 2014), implying that

$$\tilde{\psi} = \frac{\tau}{\rho_0 f} + k\left(-\frac{b_r}{b_z}\right)^n = 0. \tag{11}$$

Surface stress at a particular location sets only the halocline slope, not its depth. The halocline slope defines the baroclinically unstable azimuthal currents (via the thermal wind relation) that generate eddies to locally oppose the Ekman pumping.

Note that the Beaufort Gyre surface stress is on average anticyclonic ($\tau < 0$), and hence the halocline is deeper in the interior, the isopycnal slope $b_r/b_z < 0$, and $\psi^* > 0$. Given a surface stress profile, the halocline deepening across the gyre can be determined by integrating Eq. (11):

$$\Delta h = \int_0^R \left[\frac{-\tau(r)}{\rho_0 f k}\right]^{1/n} dr. \tag{12}$$

Equation (12) is identical to the expression for the ACC depth in a theory developed by Marshall and Radko (2003). Assuming the power $n = 2$, and considering a special case of uniform Ekman pumping [corresponding to $\tau(r) = -\hat{\tau}r/R$], the halocline deepens by

$$\Delta h = \frac{2}{3}R\left(\frac{\hat{\tau}}{\rho_0 f k}\right)^{1/2}. \tag{13}$$

3. Idealized Beaufort Gyre model

We implement an idealized model of the Beaufort Gyre as was developed in MS16. It consists of a

cylindrical ocean basin (diameter 1200 km, depth 800 m) driven by an anticyclonic surface stress $\tau(r)$. The primitive equations are solved using the Massachusetts Institute of Technology General Circulation Model (MITgcm; Marshall et al. 1997b,a; Adcroft et al. 2016) in its three-dimensional, hydrostatic configuration, with a 4-km horizontal resolution that is sufficient to permit Rossby deformation scale eddies. The deformation radius is about 20 km in our simulations (see more details in appendix A of MS16). For simplicity, the present configuration uses a flat bottom basin; MS16 included a continental slope.

Here, we focus on how surface stress and mesoscale eddies influence the isopycnal distribution in the Beaufort Gyre and hence the surface buoyancy forcing is neglected. Within our idealized gyre model, we prescribe a fixed-buoyancy boundary condition at the coastal boundaries (via fast restoring to a given profile) and no-flux conditions at the surface and bottom. The boundary conditions aim to represent the unresolved dynamics that occur over the shallow shelves as well as the water mass exchanges with other basins. We note, however, that these coastal dynamics can in general depend on the surface stress, which causes upwelling and boundary mixing (Woodgate et al. 2005; Pickart et al 2013).

The implemented, fixed-buoyancy boundary conditions imply that there exists an infinite reservoir of surface freshwater and bottom salty waters that the gyre is allowed to draw upon. The infinite water mass reservoir represents dynamics only on sufficiently long time scales that allow for the continental shelf water masses to be replenished. Our idealized study does not include the processes of water mass formation and exchange at the boundaries, instead focusing on the long-term, wind-driven halocline dynamics in the interior of the gyre. Nevertheless, once the understanding of internal gyre dynamics is gained, the use of simplifying boundary conditions in the numerical model (and in analytical analysis) can be relaxed to include more realistic boundary processes.

Spinup simulations were initialized with a horizontally uniform stratification (50-m initial halocline depth) forced by a uniform constant in time Ekman pumping (corresponding to a linear surface stress profile $\tau_0 = -\hat{\tau} r/R$). The mean state simulations were spun up for at least 50 yr to ensure equilibrium. The following wind stress amplitudes were used: $\hat{\tau} = \{0.005; 0.01; 0.015; 0.03; 0.05; 0.075\}\,\mathrm{N\,m^{-2}}$; we consider $\hat{\tau} = 0.015\,\mathrm{N\,m^{-2}}$ as a reference run representative of the present-day Beaufort Gyre. Perturbation experiments that are described in the following sections use spatially inhomogeneous and time-dependent Ekman pumping.

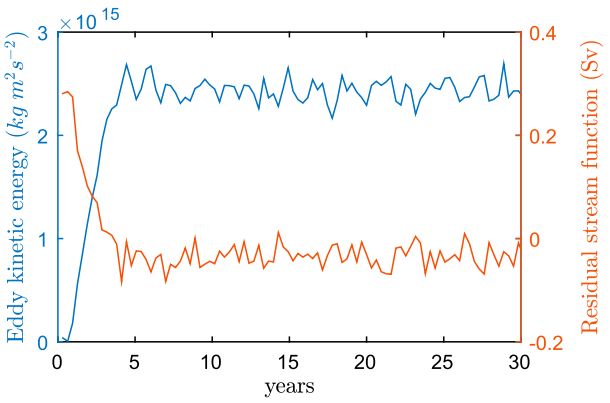

FIG. 2. Time series of the gyre-integrated eddy kinetic energy (blue) and a corresponding residual circulation (red). The residual circulation was calculated using diagnosed thickness fluxes in buoyancy coordinates (see appendix B in MS16) and averaged radially between 450 and 550 km over the halocline layer bounded by salinities 30 and 32.5. Note that the amplitude of $\tilde{\psi}$ is significantly reduced as the gyre spins up.

Following the growth of mesoscale eddies; this idealized Beaufort Gyre model achieves a statistically steady state that coincides with a vanishing residual circulation (Fig. 2). Thus, mesoscale eddies provide a mechanism to arrest the deepening of the halocline. We argue below that eddies are also key to the temporal response of the halocline to surface stress perturbations.

4. Mesoscale eddy diffusivity

The theoretical predictions of the gyre state rely on the relevance of the mesoscale eddy parameterization that uses an a priori unknown parameter k that is directly related to the mean state eddy diffusivity K_0. To ensure consistency, we diagnose the eddy diffusivity using several different methods based on our theoretical predictions.

We start with a direct estimate of diffusivity using the eddy buoyancy fluxes [see Eq. (9)] of the equilibrated gyre simulation for a reference run:

$$K_0^*(r,z) = -\frac{\overline{v'b'}}{\overline{b}_r}, \tag{14}$$

where the overbar represents both temporal and azimuthal averaging and primes are the deviations from this mean. The eddy diffusivity for a reference Beaufort Gyre simulation that has a relatively weak forcing ($\tau_0 \sim 0.015\,\mathrm{N\,m^{-2}}$) ranges between 100 and $500\,\mathrm{m^2\,s^{-1}}$ (Fig. 3a). With the exception of the near-coastal boundary layer, the diffusivity increases toward the gyre edges where the halocline slope (and hence the baroclinicity of the currents) is higher, which is consistent with

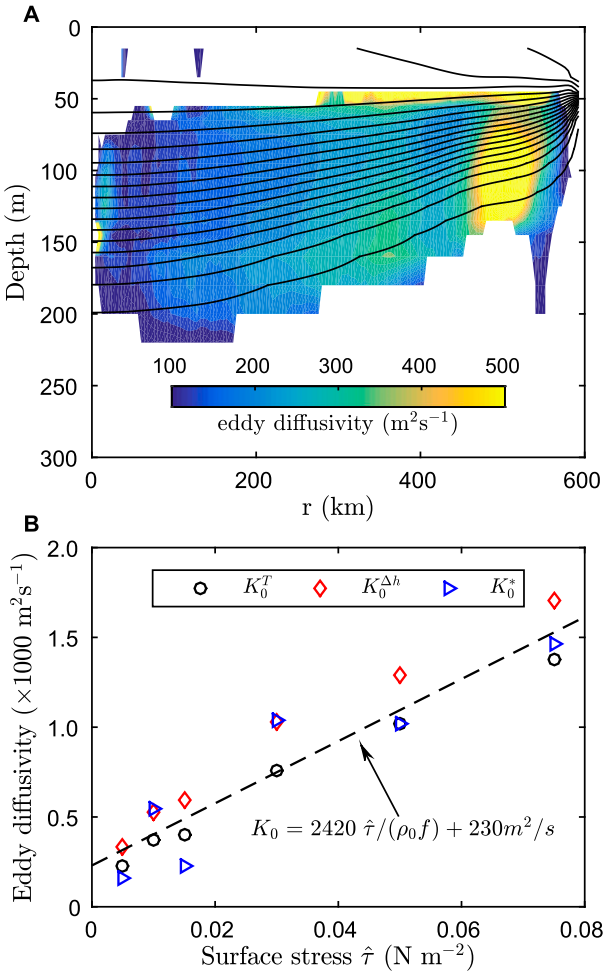

FIG. 3. (a) Spatial distribution of the equilibrium eddy diffusivity $K_0^* = -\overline{v'b'}/\overline{b}_r$ [Eq. (14)] as diagnosed from the eddy-resolving model for the reference run ($\hat{\tau} = 0.015\,\mathrm{N\,m^{-2}}$). Contours show equally spaced mean state isohalines with a salinity increment of 0.25. In weakly stratified regions shown in white, the calculation of eddy diffusivity is not appropriate as the buoyancy gradient is close to zero there. The isopycnal slope in the top 50 m is reversed due to a presence of vertical mixing. (b) Dependence of various definitions of the eddy diffusivity K on the magnitude of the surface stress. K_0^T [black circles, Eq. (29)] and $K_0^{\Delta h}$ [red diamonds, Eq. (15)] are inferred from the diagnosed gyre adjustment time and the mean halocline depth, respectively; K_0^* [blue triangles, Eq. (14)] are diagnosed from the model (averaged between 400 and 450 km within the halocline layer). A linear fit to all the data points corresponds to $K_0 = 2420[\hat{\tau}/(\rho_0 f)] + 230\,\mathrm{m^2\,s^{-1}}$ (black dashed line).

our eddy parameterization [Eq. (10)]. The halocline appears rather thick in the figure because of the spatial and temporal averaging of the thickness variations represented by the mesoscale eddies. The halocline is typically 50 m thick locally in space and time.

Using analytical predictions [Eq. (13)], we can also infer the mesoscale eddy diffusivity necessary to support the simulated halocline deepening as

$$K_0^{\Delta h}(\hat{\tau}) = \frac{2}{3}\frac{\hat{\tau}}{\rho_0 f}\frac{R}{\Delta h(\hat{\tau})}, \tag{15}$$

where we assumed an eddy parameterization power $n = 2$ (i.e., $K = ks$) as in Visbeck et al. (1997) and a characteristic slope was taken near the edge of the gyre $s = [\hat{\tau}/(\rho_0 fk)]^{1/n} = 1.5\Delta h/R$. Both Eqs. (14) and (15) produce similar eddy diffusivity estimates (Fig. 3b); they also show a similar sensitivity to surface stress forcing. These inferred eddy diffusivities should be thought of as bulk values representative of the gyre as a whole; the instantaneous values can differ depending on location and time. Note that because $s \sim \Delta h/R \sim \tau^{1/2}$, the definition of K in Eq. (15) is consistent with our assumed parameterization $K \sim s$.

According to Visbeck et al. (1997), the coefficient $k = cNl^2$, where $c = 0.015$ is an empirical constant, N is the stratification parameter ($N \approx 130f$ in our simulations), and l is the width of the baroclinic zone. Taking estimates for the diffusivity $K = 300\,\mathrm{m^2\,s^{-1}}$ and the slope $s = 10^{-4}$, we find $k = 3 \times 10^6\,\mathrm{m^2\,s^{-1}}$, which implies that $l \approx 150$ km, using the same value for the empirical constant c as in Visbeck et al. (1997). Note that the estimated size of the baroclinic zone l is less than the gyre radius. This is qualitatively consistent with the numerical experiments showing intense eddy generation near the edges of the gyre and not near its center where the halocline slope is negligibly small.

The eddy diffusivity K increases with the surface stress following a nearly linear relationship (Fig. 3b) with the rate of increase of about $170\,\mathrm{m^2\,s^{-1}}$ per $0.01\,\mathrm{N\,m^{-2}}$ increase in $\hat{\tau}$. This linear increase implies that the eddy saturation regime would be reached for strong forcing, that is, for a sufficiently strong surface stress the halocline slope would approach a critical value because $Ks = \tau/(\rho_0 f)$ and $K \sim \tau$. A corresponding halocline deepening is saturated at about $\Delta h \approx 150$ m. The eddy saturation phenomenon has been extensively discussed in the ACC, where the baroclinic transport is only weakly sensitive to changes in the strength of the surface westerlies (e.g., Hallberg and Gnanadesikan 2001; Meredith et al. 2004; Munday et al. 2013). In contrast, because of the relatively weak forcing, the Beaufort Gyre is far from the eddy saturation limit and is highly sensitive to the surface stress (MS16). Thus, significant gyre variability should be expected in response to transient forcing.

5. Transient TEM equations

Now that we have developed a basic understanding of the mesoscale eddy response to forcing and confirmed the appropriateness of the eddy parameterization, we

proceed to explore the implications for the transient gyre dynamics. Combining the expressions for the Eulerian and the parameterized eddy streamfunctions, the evolution equation for buoyancy is

$$b_t + \frac{1}{r}(\tilde{\psi} r)_r b_z + \tilde{\psi}_z b_r = \overline{S}, \quad \text{and} \tag{16}$$

$$\tilde{\psi} = \frac{\tau}{\rho_0 f} + k\left(-\frac{b_r}{b_z}\right)^n. \tag{17}$$

This nonlinear equation is relevant to the interior of the gyre and is subject to the appropriate boundary and initial conditions:

$$b|_{r=R} = b_0(z), \quad b_r|_{r=0} = 0, \quad \text{and} \tag{18}$$

$$b_z|_{z=0,H} = 0, \quad b|_{t=0} = b_0. \tag{19}$$

Scaling analysis

It is insightful to consider a scaling analysis for the gyre dynamics. On one hand, the system approaches equilibrium on an eddy diffusion time scale defined as $T \sim R^2/K$, where eddy diffusivity $K \sim k(h/R)^{n-1}$ depends on the unknown halocline depth. Diffusive scaling implies that a deeper halocline would have larger eddy diffusivity and would thus equilibrate faster. On the other hand, the isopycnal depth h together with the Ekman pumping velocity define a vertical advection time scale $T \sim h/w_e$, where $w_e \sim \hat{\tau}/(\rho_0 fR)$ is the Ekman pumping. Since the dominant balance is achieved between the vertical Ekman pumping of freshwater and its horizontal diffusion due to eddy transport, the two mechanisms have to operate on a similar time scale. Following MS16, the two time scales can be equated to obtain a scaling for the halocline depth and the adjustment time scale:

$$\Delta h \sim R\left(\frac{\hat{\tau}}{\rho_0 fk}\right)^{1/n}, \quad \text{and} \tag{20}$$

$$T \sim \frac{R^2}{k}\left(\frac{\hat{\tau}}{\rho_0 fk}\right)^{(1-n)/n}. \tag{21}$$

The expressions above imply that stronger pumping would lead to a deeper halocline with a faster adjustment time scale (a more stable gyre). In addition, both scaling laws explicitly depend on the eddy efficiency; for smaller k, the halocline would be deeper and the adjustment time scale longer (a less stable gyre). MS16 show that these scaling laws hold for a wide range of surface stress forcing, and we confirm Eqs. (20) and (21) for the case of no topography under consideration here (Fig. 4).

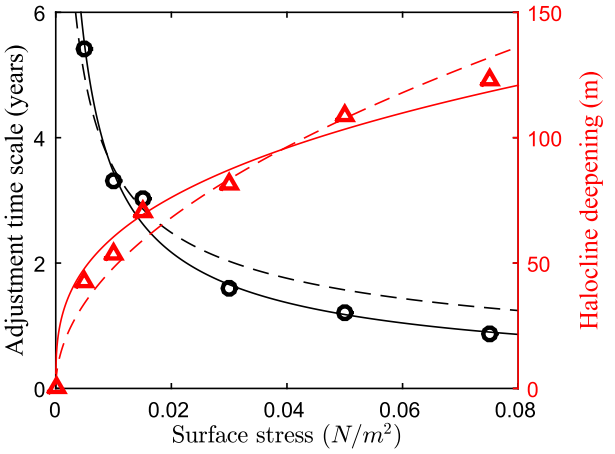

FIG. 4. Equilibrium halocline deepening across the gyre (red y axis) and its e-folding adjustment time scale diagnosed from the spinup simulations (black y axis) plotted as functions of the mean surface stress forcing (linear surface stress profile was used $\tau(r) = -\hat{\tau}r/R$). Theoretical scaling predictions are shown in solid lines for the power $n = 3$ and in dashed lines for $n = 2$ [see Eqs. (20)–(21)]. Each symbol is diagnosed from a numerical model run with different surface stress.

Depending on the choice of the power n, there can be major qualitative differences in the gyre sensitivity to forcing. Thus, $n = 1$, equivalent to a constant eddy diffusivity, results in an equilibration time scale that is independent of the surface forcing and a halocline depth that scales linearly with the surface stress (implying there is no eddy saturation). This provides a poor representation of the simulated gyre dynamics. Differences between $n = 2$ and $n = 3$ would manifest only for a sufficiently wide range of forcing magnitudes. For the range of forcing relevant to the Arctic Ocean ($\tau \lesssim 0.1\,\mathrm{N\,m^{-2}}$), $n = 2$ and $n = 3$ produce similar results (Fig. 4). Note, that the power n is not a priori constrained to be an integer.

6. Gyre equilibration and stability

In this section, we derive analytical time-dependent solutions for the halocline depth.

a. Linear dynamics near equilibrium

We assume that for a given mean surface stress $\tau_0(r)$ there exists a steady state corresponding to a long-term time average (i.e., over time scales much longer than the gyre spinup time). We then assume that Ekman pumping perturbations lead to sufficiently small buoyancy perturbations for which a linearization of the full nonlinear equation set [Eq. (16)] is appropriate. In other words, we explore the transient gyre dynamics where isopycnal depth perturbations can be considered small compared to their time-averaged state.

The linearized equations for the evolution of halocline depth anomalies h (see derivation in appendix A) result in a diffusion equation forced by Ekman pumping:

$$h_t = \underbrace{\frac{1}{r}(nK_0 r h_r)_r}_{\text{Eddy diffusion}} + \underbrace{\frac{1}{r}\left(r\frac{-\tau}{\rho_0 f}\right)_r}_{\text{Ekman pumping}}. \tag{22}$$

Here, τ is the surface stress perturbation from its mean value τ_0, and $K_0(r)$ is a background eddy diffusivity set by the mean isopycnal slope as

$$K_0 = k s_0^{n-1} = k\left[\frac{-\tau_0(r)}{\rho_0 f k}\right]^{(n-1)/n}. \tag{23}$$

The first term on the right-hand side of Eq. (22) acts to diffuse the isopycnal depth perturbations with a space-dependent diffusivity equal to nK_0; the prefactor n appears for a linear problem because of the a power-law dependence of eddy diffusivity on the slope (see appendix A). This representation of mesoscale eddies as thickness diffusivity is analogous to the expression in, for example, Gent and Mcwilliams (1990) and Su et al. (2014). The second term is the perturbation in Ekman pumping w_e that acts as a forcing for the isopycnal depth:

$$w_e = \mathrm{curl}\left(\frac{-\tau}{\rho_0 f}\right) = \frac{1}{r}\left(r\frac{-\tau}{\rho_0 f}\right)_r. \tag{24}$$

Thus, consistent with the mean state dynamics, it is an imbalance between the eddy diffusion and Ekman pumping that drives the halocline depth perturbations.

b. Gyre adjustment time scale

One of the most important quantities that describe the gyre dynamics is its stability, that is, the adjustment time scale associated with the exponential decay of perturbations. In this section, we explore the impact of eddies on this adjustment.

Given any radial profile of the anticyclonic mean surface stress $[\tau_0(r)]$ one can calculate the background diffusivity $K_0(r)$ [from Eq. (23)] and the eigenfunctions h_i^* with corresponding eigenvalues $T_i^{-1} > 0$ for the eddy diffusion operator:

$$\frac{1}{r}[rK_0(r)h_{ir}^*]_r = -\frac{h_i^*}{T_i}. \tag{25}$$

Here, homogeneous boundary conditions $h(R) = 0$ and $h_r(0) = 0$ should be used (see appendix A). Since this diffusion operator is self-adjoint [for an r-weighted norm and $K_0(r) > 0$], any halocline depth perturbation can be decomposed into contributions from its orthogonal eigenmodes $[h(r)_i^*]$ as

$$h = \sum_{i=1}^{\infty} a_i(t) h_i^*, \tag{26}$$

where we sort the eigenfunctions corresponding to their eigenvalues starting from the smallest (their indices correspond to the number of zero crossings). Thus, the first eigenfunction corresponds to a large-scale halocline deepening, whereas higher eigenmodes are more oscillatory in space and correspond to higher eigenvalues, discussed more below.

In an unforced case (i.e., Ekman pumping perturbations $w_e = 0$), the amplitudes $a_i(t)$ would evolve independently from each other according to a simple exponential decay law:

$$\frac{da_i}{dt} = -\frac{a_i}{T_i}. \tag{27}$$

This result confirms our a priori assumption about the gyre being a stable system [see Eq. (1) and related discussions]. Eigenvalues represent the inverse of the decay time scales T_i for each eigenmode. For a general perturbation that may consist of many different modes, the gyre would equilibrate on a time scale corresponding to the longest one among all the possible modes:

$$T_0 = \frac{1}{n\lambda}\frac{R^2}{K_0(R)}. \tag{28}$$

Here, λ is a positive dimensionless constant that arises as a solution of the discussed eigenvalue problem. Note that the eigenvalues depend on boundary conditions; however, for diffusion operators they grow rapidly (roughly quadratically) with the number of zero crossings of the corresponding eigenfunction. This implies that the spinup time scale observed in the numerical model corresponds to a decay of the large-scale gyre mode, whereas small-scale spatial perturbations in the halocline depth would decay much faster.

For a linear surface stress profile used in our reference gyre simulation ($\tau_0 \sim r$), we obtain $\lambda = \{5.7, 4.7, 4.3\}$ for powers $n = \{1, 2, 3\}$, respectively. While the expression for the gyre adjustment time [Eq. (28)] is consistent with the scaling laws [Eq. (21)], here we determined the multiplicative prefactor $(n\lambda)^{-1} \approx 0.1$, which turns out to be an order of magnitude smaller than 1.

Using the gyre adjustment time scale diagnosed from the spinup time series (Fig. 4 black circles), we can infer an appropriate eddy diffusivity that can generate such a time scale as

$$K_0^T(\hat{\tau}) = \frac{1}{\lambda n}\frac{R^2}{T_0(\hat{\tau})}, \tag{29}$$

where $n = 2$ and a corresponding $\lambda = 4.7$ are used [see Eq. (28)]. Using the diagnosed equilibration time scale T_0 (Fig. 4), we calculate the corresponding eddy diffusivity based on Eq. (29) above and plot in Fig. 3b (black circles). This diffusivity estimate is consistent with the one inferred from the bulk halocline deepening [Eq. (15)] as well as with the one directly diagnosed from the eddy buoyancy fluxes [Eq. (14)]. A good agreement between the three independent methods (Fig. 3b) provides strong support for the validity of our theory that draws direct connections between eddy diffusivity, halocline depth, and gyre stability or equilibration time scale.

7. FWC response to Ekman pumping

Defined as a linear measure of column salinity with respect to a reference salinity $S_{\rm ref}$, the amount of freshwater (FW) can be approximated as

$$\mathrm{FW} \equiv \int_{-H}^{0} -\frac{S(z) - S_{\rm ref}}{S_{\rm ref}}\, dz \approx \frac{\Delta S}{S_{\rm ref}} h, \qquad (30)$$

where the integration is to a depth H of a reference isohaline. The FW is proportional to the halocline depth h and to the bulk vertical salinity difference ΔS and thus can be altered either via water mass modification or via changes in halocline depth. Note that the presence of vertical mixing cannot significantly affect FWC unless it diffuses salt up from below the reference salinity. Mixing can become important in cases with weak forcing when the halocline becomes thin (Spall 2013).

Using the approximation of Eq. (30), it can be deduced that the FWC, defined as an area-integrated amount of freshwater, is proportional to the volume V of water above the halocline:

$$\mathrm{FWC} \approx \frac{\Delta S}{S_{\rm ref}} V, \quad \text{where} \quad V = 2\pi \int_0^R rh\, dr. \qquad (31)$$

Building on the linear relationship between FWC and V, verified in the numerical model (see Fig. 5), we continue our exploration of the forced freshwater volume dynamics. In diagnosing V from the numerical model, we defined the halocline depth h via the location of the 32.25 isohaline; the relative top-to-bottom salinity difference $\Delta S/S_{\rm ref} \approx 5/34$ is essentially prescribed through boundary conditions. In general, the temporal evolution of FWC would also depend on water mass modifications that affect surface and middepth salinities.

a. Spatially inhomogeneous Ekman pumping

Here, we address the following question: Among all the possible Ekman pumping distributions, which one is most efficient in changing the FWC? We thus consider the evolution of halocline volume V under spatially inhomogeneous Ekman pumping.

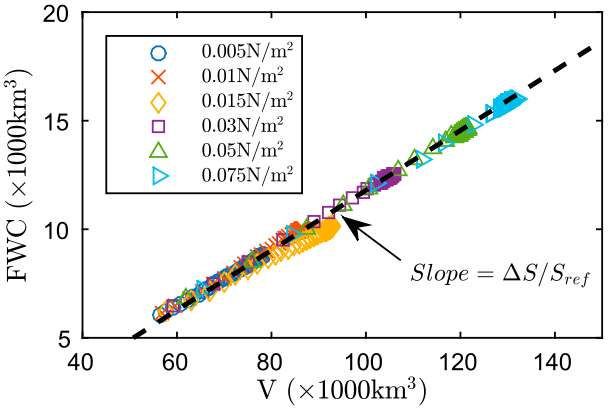

FIG. 5. Freshwater volume and freshwater content plotted against each for the spinup time series of different numerical model experiments. Dashed line shows a slope of $\Delta S/S_{\rm ref}$ supporting Eq. (31).

Projecting Eq. (22) onto the ith eigenmode, we obtain that each amplitude $a_i(t)$ is forced by the Ekman pumping projection w_i onto a corresponding eigenfunction h_i^* (plotted in Fig. 6a), such that

$$\frac{da_i}{dt} h_i^* = -\frac{a_i}{T_i} h_i^* + w_i. \qquad (32)$$

An area integral of Eq. (32) results in an evolution equation for the corresponding halocline volume V_i:

$$\frac{dV_i}{dt} = -\frac{V_i}{T_i} + W_E, \qquad (33)$$

where W_E is the area-integrated Ekman pumping, that is, the Ekman transport. The equation above demonstrates the stability of the gyre in terms of the decay of its halocline volume anomalies, which supports our a priori stability assumption [see Eq. (1) and discussions thereof].

Since we are considering Ekman pumping perturbations that have the same Ekman transport, a steady-state volume anomaly is directly proportional to the corresponding time scale $V_i = W_E T_i$ [Eq. (33)]. In turn, the time scales T_i reduce rapidly in magnitude with their index:

$$\frac{T_i}{T_0} \ll 1 \quad \text{for} \quad i \geq 1. \qquad (34)$$

For example, for the eigenfunctions plotted in Fig. 6, $T_1/T_0 = 0.23$ and $T_2/T_0 = 0.1$, implying that V_0 is at least an order of magnitude larger. Thus, the most dominant contribution to freshwater content would be due to the Ekman pumping pattern of the gravest eigenmode

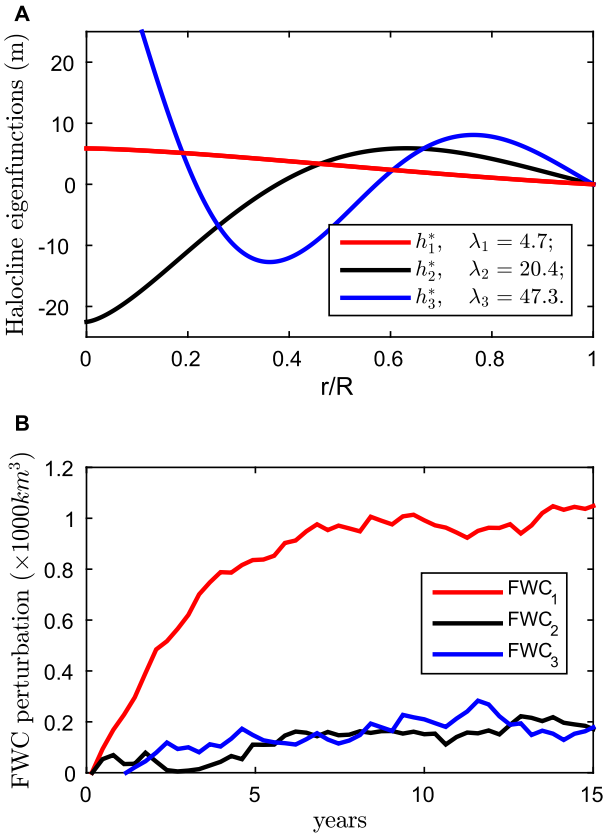

FIG. 6. (a) First three halocline depth eigenfunctions; the legend shows their corresponding nondimensional eigenvalues that grow rapidly with the number of zero crossings. (b) Response of freshwater content to the mentioned surface stress profiles as simulated by the eddy-resolving numerical model (blue, black, and red correspondingly). Note that all stress perturbation had the same magnitude of area-averaged Ekman pumping. Perturbations were made on a control run.

(i.e., gyre-scale anticyclonic surface stress pattern as shown in Fig. 6a, red). Eddy diffusion is efficient in damping the response to spatially inhomogeneous Ekman pumping. This occurs because highly oscillatory eigenmodes induce large halocline slopes (see Fig. 6a), which quickly produce strong mesoscale transport that acts to damp them.

We now test this theoretical prediction within the eddy-resolving gyre model. We have perturbed the gyre from its equilibrium state by increasing the Ekman pumping with patterns corresponding to the first three eigenmodes (radial distributions as in Fig. 6a). Ekman transport perturbation amplitudes are 25% compared to the equilibrated state transport. Note that all three perturbations have the same value of the area-averaged Ekman pumping, and yet the theory predicts that the corresponding FWC responses should be dramatically different.

The numerical model, in agreement with the theory, shows that the FWC increases substantially more for the large-scale Ekman pumping pattern (Fig. 6b, red) and virtually does not increase for the spatially inhomogeneous pumping (Fig. 6b, blue and black). This confirms that only large-scale Ekman pumping can efficiently contribute to changes in FWC.

By moving beyond the steady-state solutions considered earlier, the transient dynamics reveal which Ekman pumping modes provide the most efficient forcing. Nonlinearity (not accounted for in our transient theory) might be important in determining the halocline depth anomalies that are large in amplitude, especially near the center of the domain (Fig. 6a). However, changes near the center of the domain do not substantially contribute to FWC as it is weighted by area, meaning that changes are more important at the edges.

b. *Periodic Ekman pumping*

Here, we explore the response of FWC to periodic Ekman pumping. Modes with smaller-scale spatial variability are damped more efficiently by eddies [Eq. (33)], such that the overall halocline volume anomaly is largely determined by the volume of the first eigenmode:

$$V = \sum_{i=0}^{\infty} V_i \approx V_0 . \tag{35}$$

The volume anomalies thus obey a simple equation of a damped-driven system that approaches equilibrium with an e-folding time scale T_0:

$$\frac{dV}{dt} = -\frac{V}{T_0} + W_E \sin\omega t . \tag{36}$$

A similar equation and role of eddies was found for transient dynamics of the thermohaline circulation by Spall (2015). Note that here we consider the gyre forced by the most efficient large-scale Ekman pumping pattern (i.e., $w_e = w_0 h_0^*$). In general, W_E would be the transport associated only with the Ekman pumping projection onto the first eigenfunction w_0 as the portions of the transport associated with larger eigenvalue projections would insignificantly contribute to changes in volume.

Solving the equation above, we find that the halocline volume, after an initial adjustment, approaches a simple periodic solution lagged with respect to the forcing by a phase ϕ:

$$\frac{V}{W_E T_0} = \frac{1}{\sqrt{1 + (\omega T_0)^2}} \sin(\omega t - \phi), \quad \text{and} \tag{37}$$

$$\phi = \arctan(\omega T_0). \tag{38}$$

Using the equilibrated control simulation, we apply oscillating Ekman pumping forcing with a 25%

amplitude with respect to its mean value (the large-scale spatial pattern does not change in time). The normalized freshwater volume amplitude and its phase lag are diagnosed from the model and are shown in Fig. 7 (crosses). The eddy-resolving model is in close agreement with our theoretical predictions based on the adjustment by mesoscale eddy diffusion.

The time scale T_0 represents a transition in the system from a one-dimensional to a three-dimensional response. If the eddies were unimportant to the dynamics [a limit of infinitely large adjustment time scale T_0 in Eqs. (37)–(38)], the volume perturbations would have been inversely proportional to the frequency of the Ekman pumping ($V = W_E/\omega$) and the phase lag would have been a quarter of a period for all frequencies ($\phi = \pi/2$). This limit is relevant for high-frequency forcing, where eddies have insufficient time to respond to changes in Ekman pumping; the gyre response in this case is entirely due to the Ekman advection. However, the freshwater volume amplitude is maximized for slowly oscillating forcing where it is more in phase with the forcing (Fig. 7). In this regime the eddy transport nearly compensates for the Ekman pumping. The response amplitude diagnosed from the numerical model is slightly larger than the analytical prediction (Fig. 7a) due to a presence of internal modes of the gyre variability excited by the forcing.

The time scale $T_0 \approx 2.1$ yr that was used in the theory [Eqs. (38)–(37)] was estimated from bulk gyre sensitivity to forcing as

$$T_0 = \left.\frac{\Delta V}{\Delta W_E}\right|_{\tau_{\text{ref}}}, \tag{39}$$

where ΔV is an equilibrium change in freshwater volume corresponding to an increase of Ekman transport by ΔW_E. This time scale represents the gyre stability to small perturbations around its equilibrium state. It is slightly smaller than the 3-yr nonlinear adjustment time scale that was diagnosed from the spinup time series (Fig. 4).

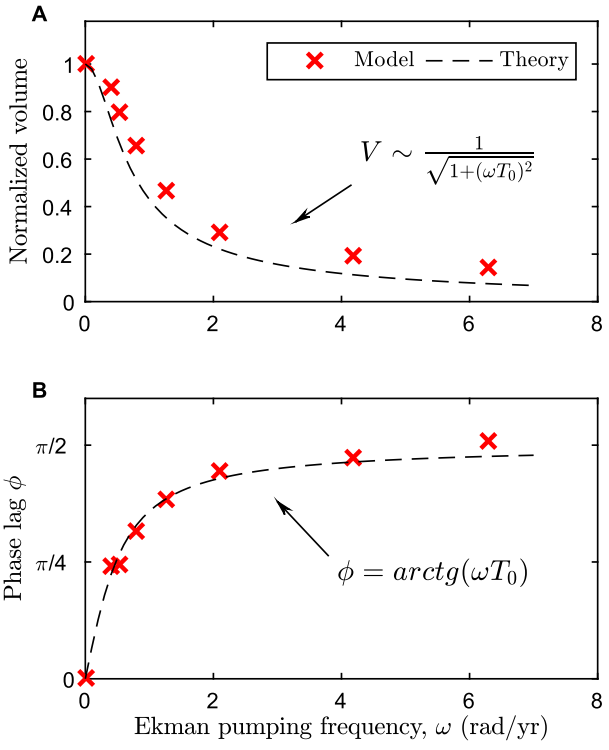

FIG. 7. Amplitude-phase response of the gyre freshwater content to periodic Ekman pumping. (a) Normalized amplitude of volume oscillations [see Eq. (37)]. (b) Corresponding phase delay relative to the oscillating Ekman pumping [Eq. (38)].

$$\frac{dV}{dt} = \int_0^R 2\pi r \frac{dh}{dt} dr = 2\pi R \left(nK_o s + \frac{-\tau}{\rho_0 f} \right) \Bigg|_{r=R}, \tag{40}$$

where the halocline slope s and surface stress τ are perturbations from the mean state. Here, we made use of the Stokes theorem for the Ekman pumping term and integration by parts for the eddy diffusion term.

Taking into account that the top-to-bottom salinity difference is constant throughout our simulations, we can define the GI that closely approximates FWC tendency as

$$\text{GI} = 2\pi R \frac{\Delta S}{S_{\text{ref}}} \left[\underbrace{nK_0(R)s(R)}_{\substack{\text{Eddy} \\ \text{transport}}} + \underbrace{\frac{-\tau(R)}{\rho_0 f}}_{\substack{\text{Ekman} \\ \text{transport}}} \right], \tag{41}$$

where we have made use of Eq. (31) (s and τ are perturbations from their mean values, while K_0 is the eddy diffusivity of the mean state). The GI approach is

8. Predicting FWC using the Gyre Index

Here, we propose a novel FWC tendency diagnostic—the Gyre Index—that predicts the freshwater content and includes both the effects of wind forcing and eddies.

a. The Gyre Index

We take Eq. (22) for the halocline perturbation and integrate it over the surface area of the gyre to obtain an evolution equation for the changes in the volume of water above the halocline:

analogous to conventional freshwater budget calculations with an additional eddy transport term. Thus, GI > 0 implies that the gyre is gaining FWC and GI < 0 implies the gyre is losing FWC. The magnitude of the GI should be compared to the maximum FWC flux out of the gyre $\mathrm{FWC}/T_0 \sim \tau/(\rho_0 f)$ that is proportional to the Ekman transport and is independent of the eddy diffusivity [see Eqs. (21) and (20)]. We can also interpret the GI as being a measure of how far the gyre is from its equilibrium state. In equilibrium, the eddy and Ekman transports are compensated resulting in GI = 0, the limit of a vanishing residual circulation.

Because both terms in the GI are evaluated at the gyre boundary [Eq. (41)], the FWC tendency depends explicitly only on the boundary processes. On one hand, the mesoscale eddies can only redistribute the halocline thickness within the gyre without affecting the total FWC unless there are eddy thickness sources at the boundaries. On the other hand, because of Stokes theorem, the area-integrated Ekman pumping is proportional to the contour integral of surface stress around the gyre boundaries. Thus, any spatially localized anomaly in Ekman pumping can only affect the halocline depth locally and changes in FWC would depend only on the existence of a surface stress along the boundaries.

b. *Diagnostic power of the Gyre Index*

We now proceed to investigate the extent to which the GI can approximate FWC tendency within the eddy-resolving numerical model. We simulate the gyre variability by applying time-dependent, spatially homogeneous Ekman pumping. Its amplitude evolves according to a red noise process with a memory parameter of 1 yr to mimic observations that show enhanced variability on interannual to decadal time scales (Proshutinsky et al. 2009); time series are shown in Fig. 8a. The surface stress perturbations from the reference run have a variance of 25% with respect to the mean value of $\hat{\tau} = 0.015\,\mathrm{N\,m^{-2}}$ (the reference case that we use for the Beaufort Gyre). The corresponding FWC undergoes significant variations of about $3000\,\mathrm{km^3}$ on decadal time scales (Fig. 8a, red curve).

We then compute the Gyre Index by diagnosing the azimuthally averaged halocline slope perturbation $s(t, R)$ and the generated surface stress $\tau(t, R)$ at the gyre boundary [Eq. (41)]. Because we use stochastic in time Ekman pumping perturbations, the time series have large variances at short time scales (Fig. 8a). To illustrate its differences with the purely Ekman pumping-based index, we evaluate the performance of the Gyre Index on various time scales. In Fig. 8b, we compare FWC tendency and the GI for which a 5-yr running mean smoothing has been applied in order to explore the interannual trends characteristic of the Beaufort high variability. Using only the Ekman pumping as an index (i.e., excluding the eddy transport term in the GI) does not give an accurate representation of FWC tendency (note the large differences between red and black curves in Fig. 8b). In contrast, the GI provides a much better agreement with the numerically simulated FWC evolution (Fig. 8b), further supporting our theory of the gyre variability.

We quantify the performance of the GI by calculating the root-mean-square error as a function of the length of the running mean window used to smooth the time series (Fig. 8c). We see that the Ekman-only predictor of FWC tendency provides a good match only on short time scales where eddy activity is less important. However, on interannual and longer time scales, it is necessary to account for the eddy activity as the Ekman predictor error becomes larger than the standard deviation of the FWC tendency. This implies that at interannual and longer time scales assuming no change in FWC gives a better prediction than only taking into account the Ekman pumping. In contrast, the GI has a strong predictive capability on all time scales with its error persistently smaller than the standard deviation of the FWC tendency (Fig. 8c).

A calculation of GI requires the background eddy diffusivity evaluated at the boundary [Eq. (41)]. We show that there exists an optimal eddy diffusivity that minimizes error of the GI making it a factor of 2 smaller than that of the Ekman index alone (see Fig. 8d). The optimal value of $K_0 \approx 300\,\mathrm{m^2\,s^{-1}}$ is in a range of values diagnosed earlier using the three other independent methods (see Fig. 3b).

In section 7a, we demonstrated that only large-scale variations in Ekman pumping significantly affect FWC. Yet the GI, which accurately predicts variability of FWC, does not contain information about the horizontal scale of the Ekman pumping. Instead, it only uses the Ekman transport, which is the area-integrated Ekman pumping. This implies that for highly inhomogeneous Ekman pumping (higher eigenmodes), the GI ≈ 0, and hence there should be a strong compensation between the eddy transport at the boundary and the Ekman transport.

9. Summary and discussion

We explored the transient dynamics of an idealized Beaufort Gyre in an eddy-resolving general circulation model with particular emphasis on the FWC variability. We performed a series of experiments exploring the gyre's response to a time-dependent surface stress. The

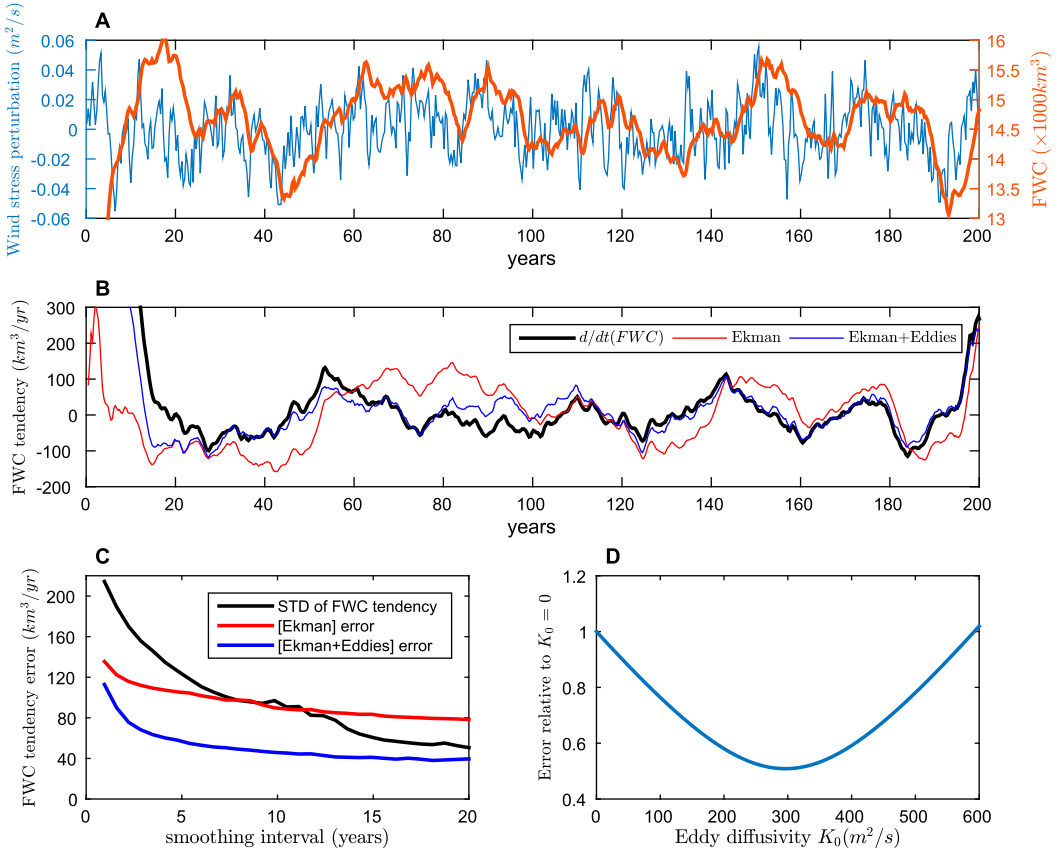

FIG. 8. (a) Response of the FWC (red) to time-dependent surface stress that has a fixed spatial pattern (same as for the control run), but its amplitude oscillates around its mean state of $0.015\,\mathrm{N\,m^{-2}}$ with a 25% variance (shown in blue). Surface stress perturbation amplitude was generated as a red noise with a 1-yr damping parameter. (b) FWC tendencies as directly estimated from the model (black), as inferred using the Ekman pumping only (red), and the Gyre Index (blue). A 5-yr running mean filter was applied to these time series. (c) Standard deviation of FWC tendency (black), error approximating it with Ekman only term (red), and error of the Gyre Index (blue) plotted as functions of the smoothing interval. (d) The dependence of error on the choice of the mesoscale eddy diffusivity showing the optimal choice of $K_0 \approx 280\,\mathrm{m^2\,s^{-1}}$ that was used for the time series shown in (b).

results were interpreted using transformed Eulerian-mean theory that explicitly includes the effects of mesoscale eddies. Using an eddy parameterization, we provide theoretical predictions for the gyre's stability (inverse of the equilibration time) as well as transient solutions for halocline and FWC evolution under time-dependent Ekman pumping.

Our model and theory neglect several processes that may be important in the real Beaufort Gyre. The theory is adiabatic and the model was run with a vertical diffusion coefficient of $10^{-5}\,\mathrm{m^2\,s^{-1}}$. Observations indicate that diapycnal mixing is spatially and temporally inhomogeneous but, on average, between 10^{-6} and $10^{-5}\,\mathrm{m^2\,s^{-1}}$ (Guthrie et al. 2013). Scaling theory in MS16 suggests that the impact of diapycnal mixing is small but not negligible, especially when the surface stress is weak. We also neglect eddy salt fluxes (or thickness fluxes) that originate from eddies shed from the boundary currents that encircle the Arctic Basin (e.g., Manley and Hunkins 1985; Spall et al. 2008; Watanabe 2013). Scaling in Spall (2013) suggests that the freshwater flux carried by these eddies is of similar amplitude as that carried by the Ekman transport. It is important to note, however, that the Eulerian streamfunction associated with eddies vanishes, so they do not provide an equivalent to the Eulerian Ekman pumping velocity produced by the surface stress. We also do not represent geometric complexities such as the Eurasian Basin, continental slopes, shelf dynamics, and midocean ridges. We view the present model as representing, in a compact and transparent way, the leading-order dynamical balances for the Beaufort Gyre from which additional processes may be considered.

We now highlight four key results from this study. First, we demonstrated that the presence of mesoscale eddies directly affects the Ekman-driven gyre variability [Eqs. (33) and (37)]. By defining the gyre equilibration time scale [Eq. (28)], we provided a theoretical expression for the time scale and emphasize its explicit dependence on mesoscale eddy diffusivity [Eq. (28)].

Second, we presented several estimates of the characteristic mesoscale eddy diffusivity for the gyre, demonstrating that it grows nearly linearly with the surface stress forcing (Fig. 3). Our theory has only one a priori unknown parameter, the mesoscale eddy diffusivity, which we inferred in four ways based on the buoyancy flux [Eq. (14)], the bulk halocline deepening [Eq. (15)], the adjustment time scale [Eq. (29)], and volume transport variability (Fig. 8d). These independent methods are consistent between each other and thus provide support for the theory. For conditions akin to a present-day Beaufort Gyre, we provide an estimate of the characteristic diffusivity of about $300\,\mathrm{m^2\,s^{-1}}$ ($\hat{\tau} = 0.015\,\mathrm{N\,m^{-2}}$) and predict its sensitivity to be $170\,\mathrm{m^2\,s^{-1}}$ per $0.01\,\mathrm{N\,m^{-2}}$ increase in the azimuthal surface wind stress. These parameters should be tested against observations.

Third, motivated by a strong variability in atmospheric winds over the Beaufort Gyre, we explored a gyre response to spatially inhomogeneous and time-dependent Ekman pumping. Our analytical and numerical solutions show that among all possible stress distributions that have the same area-averaged Ekman pumping, the FWC is largely affected only by the gyre-scale Ekman pumping (Fig. 6b). The FWC response to temporally periodic Ekman pumping is closely approximated by a simple, damped-driven dynamical system that approaches equilibrium with a known adjustment time scale controlled by eddy dynamics [Eq. (28)]. High-frequency oscillations in the pumping (e.g., seasonal cycle) have little effect on halocline depth, whereas the strongest effect is achieved for low-frequency forcing (e.g., on decadal time scales; Fig. 7).

Fourth, we proposed the use of the Gyre Index [Eq. (41)] for monitoring/interpreting FWC tendency in the Beaufort Gyre. Its key advantage is that calculating the GI requires knowledge of the halocline slope and magnitude of surface stress evaluated only at the gyre boundaries (not in its interior). Using a numerical model, we demonstrated its strong predictive capability that is because it incorporates the competing effects of both Ekman pumping and mesoscale eddy transport. For interannual and longer time scales, the GI is far superior to using only the strength of Ekman pumping in evaluating the FWC tendency (Fig. 8).

The GI can be readily generalized to include effects of more realistic features of the Beaufort Gyre dynamics such as the azimuthal asymmetry in Ekman pumping and eddy diffusivities. This would require calculating a contour integral along the gyre boundaries in order to evaluate terms in the GI. Observationally, calculation of the GI could be achieved through a network of instruments located along the gyre perimeter, thus complementing the observational efforts in the interior of the gyre. We envision the GI calculation requiring observations of density and velocities from a set of moorings spaced around the gyre. Mooring observations of ocean velocity and density fields would allow for calculation of the eddy fluxes by estimating the vertical shear of the first baroclinic mode of the horizontal velocity that is directly related to horizontal halocline slope. We speculate that the GI would be a useful tool for interpreting the component of FWC variability that is related to changes in the halocline depth in both observational and modeling studies of the Beaufort Gyre.

Acknowledgments. The authors acknowledge the high-performance computing support from Yellowstone provided by NCAR's CIS Laboratory, sponsored by the NSF. GEM acknowledges the support from the Howland Postdoctoral Program Fund at WHOI and the Stanback Fellowship Fund at Caltech. MAS was supported by NSF Grants PLR-1415489 and OCE-1232389. AFT acknowledges support from NASA Award NNN12AA01C. The authors thank Prof. John Marshall and an anonymous reviewer for helpful comments and suggestions. The manuscript also benefited from discussions at the annual Forum for Arctic Modeling and Observing Synthesis (FAMOS) funded by the NSF OPP Awards PLR-1313614 and PLR-1203720.

APPENDIX

Time Evolution of Halocline Depth Perturbations

The nonlinear equation set of equations [Eqs. (16)–(17)] for the buoyancy evolution can be linearized in the vicinity of its mean state to obtain

$$b_t + \frac{1}{r}(\tilde{\psi} r)_r b_{0z} - \tilde{\psi}_z b_{0r} = 0, \tag{A1}$$

$$\tilde{\psi} = \frac{\tau}{\rho_0 f} - n\frac{\tau_0}{\rho_0 f}\frac{s}{s_0}, \quad \text{and} \tag{A2}$$

$$\frac{s}{s_0} = \left(\frac{b_r}{b_{0r}} - \frac{b_z}{b_{0z}}\right), \tag{A3}$$

where all dynamical variables are perturbations from their mean state, while 0 subscripts correspond to mean state variables. The fixed-buoyancy boundary conditions

transform into homogeneous conditions for the perturbation variables ($b = 0$ at $r = R$ and $b_r = 0$ at $r = 0$).

The linearized equation set simplifies dramatically if one writes it along the characteristics defined by the halocline depth of the mean buoyancy distribution. Equation (11) may be written in characteristic coordinates $[r(l), z(l)]$ as $b_l = b_r r_l + b_z z_l = 0$, where the homogeneous right-hand side indicates that buoyancy is conserved along the characteristic trajectory. The characteristic velocities are then

$$\frac{dz}{dl} = -\left(\frac{-\tau}{\rho_0 fk}\right)^{1/n}, \quad \frac{dr}{dl} = 1. \tag{A4}$$

The mean vertical buoyancy gradient, following the isopycnals (characteristics) defined by the mean state, does not change ($b_{0z} = \text{const}$) and can thus define a perturbation isopycnal displacement h as

$$h(l,t) = \frac{b(l,t)}{b_{0z}}. \tag{A5}$$

Taking into account that $\partial_l(\ ) = \partial_r(\ ) r_l + \partial_z(\ ) z_l$, we obtain the following system for variables following characteristics:

$$h_t = -\frac{1}{l}(\tilde{\psi} l)_l, \quad \tilde{\psi} = \frac{\tau}{\rho_0 f} - nK_0 h_l, \tag{A6}$$

where $K_0(l)$ is a background eddy diffusivity set by the isopycnal slope of the steady-state buoyancy distribution:

$$K_0 = k s_0^{n-1} = k\left[\frac{-\tau_0(l)}{\rho_0 fk}\right]^{(n-1)/n}. \tag{A7}$$

Eliminating $\tilde{\psi}$ from the equations above, we obtain an equation for the time evolution of isopycnal displacement:

$$h_t = \frac{1}{r}(nK_0 r h_r)_r + \frac{1}{r}\left(r\frac{-\tau}{\rho_0 f}\right)_r, \quad \text{and} \tag{A8}$$

$$\text{b.c.: } h|_{r=R} = 0, \quad h_r|_{r=0} = 0. \tag{A9}$$

That is now written in terms of the radial coordinate taking onto account that $r_l = 1$. The fixed-buoyancy boundary conditions for the original equations translated into the homogeneous boundary conditions for the linearized system.

REFERENCES

Adcroft, A., and Coauthors, 2016: MITgcm user manual. Accessed 25 September 2015. [Available online at http://mitgcm.org/public/r2_manual/latest/online_documents/manual.html.]

Andrews, D. G., and M. E. McIntyre, 1976: Planetary waves in horizontal and vertical shear: The generalized Eliassen–Palm relation and the mean zonal acceleration. *J. Atmos. Sci.*, **33**, 2031–2048, doi:10.1175/1520-0469(1976)033<2031:PWIHAV>2.0.CO;2.

Cole, S. T., M.-L. Timmermans, J. M. Toole, R. A. Krishfield, and F. T. Thwaites, 2014: Ekman veering, internal waves, and turbulence observed under Arctic Sea ice. *J. Phys. Oceanogr.*, **44**, 1306–1328, doi:10.1175/JPO-D-12-0191.1.

Davis, P. E. D., C. Lique, and H. L. Johnson, 2014: On the link between Arctic Sea ice decline and the freshwater content of the Beaufort Gyre: Insights from a simple process model. *J. Climate*, **27**, 8170–8184, doi:10.1175/JCLI-D-14-00090.1.

Dmitrenko, I., S. Kirillov, V. Ivanov, and R. Woodgate, 2008: Mesoscale Atlantic water eddy off the Laptev Sea continental slope carries the signature of upstream interaction. *J. Geophys. Res.*, **113**, C07005, doi:10.1029/2007JC004491.

Gent, P. R., and J. C. Mcwilliams, 1990: Isopycnal mixing in ocean circulation models. *J. Phys. Oceanogr.*, **20**, 150–155, doi:10.1175/1520-0485(1990)020<0150:IMIOCM>2.0.CO;2.

Giles, K. A., S. W. Laxon, A. L. Ridout, D. J. Wingham, and S. Bacon, 2012: Western Arctic Ocean freshwater storage increased by wind-driven spin-up of the Beaufort Gyre. *Nat. Geosci.*, **5**, 194–197, doi:10.1038/ngeo1379.

Guthrie, J. D., J. H. Morison, and I. Fer, 2013: Revisiting internal waves and mixing in the Arctic Ocean. *J. Geophys. Res. Oceans*, **118**, 3966–3977, doi:10.1002/jgrc.20294.

Haine, T. W., and Coauthors, 2015: Arctic freshwater export: Status, mechanisms, and prospects. *Global Planet. Change*, **125**, 13–35, doi:10.1016/j.gloplacha.2014.11.013.

Hallberg, R., and A. Gnanadesikan, 2001: An exploration of the role of transient eddies in determining the transport of a zonally reentrant current. *J. Phys. Oceanogr.*, **31**, 3312–3330, doi:10.1175/1520-0485(2001)031<3312:AEOTRO>2.0.CO;2.

Lique, C., H. L. Johnson, and P. E. D. Davis, 2015: On the interplay between the circulation in the surface and the intermediate layers of the Arctic Ocean. *J. Phys. Oceanogr.*, **45**, 1393–1409, doi:10.1175/JPO-D-14-0183.1.

Manley, T., and K. Hunkins, 1985: Mesoscale eddies of the Arctic Ocean. *J. Geophys. Res.*, **90**, 4911–4930, doi:10.1029/JC090iC03p04911.

Manucharyan, G. E., and M.-L. Timmermans, 2013: Generation and separation of mesoscale eddies from surface ocean fronts. *J. Phys. Oceanogr.*, **43**, 2545–2562, doi:10.1175/JPO-D-13-094.1.

——, and M. A. Spall, 2016: Wind-driven freshwater buildup and release in the Beaufort Gyre constrained by mesoscale eddies. *Geophys. Res. Lett.*, **43**, 273–282, doi:10.1002/2015GL065957.

Marshall, J., 2015: Equilibration of the Arctic halocline by eddies. *20th Conf. on Atmospheric and Oceanic Fluid Dynamics*, Minneapolis, MN, Amer. Meteor. Soc., 3.2. [Available online at https://ams.confex.com/ams/20Fluid/webprogram/Paper272340.html.]

——, and T. Radko, 2003: Residual-mean solutions for the Antarctic Circumpolar Current and its associated overturning circulation. *J. Phys. Oceanogr.*, **33**, 2341–2354, doi:10.1175/1520-0485(2003)033<2341:RSFTAC>2.0.CO;2.

——, A. Adcroft, C. Hill, L. Perelman, and C. Heisey, 1997a: A finite-volume, incompressible Navier Stokes model for studies of the ocean on parallel computers. *J. Geophys. Res.*, **102**, 5753–5766, doi:10.1029/96JC02775.

——, C. Hill, L. Perelman, and A. Adcroft, 1997b: Hydrostatic, quasihydrostatic, and nonhydrostatic ocean modeling. *J. Geophys. Res.*, **102**, 5733–5752, doi:10.1029/96JC02776.

——, H. Jones, R. Karsten, and R. Wardle, 2002: Can eddies set ocean stratification? *J. Phys. Oceanogr.*, **32**, 26–38, doi:10.1175/1520-0485(2002)032<0026:CESOS>2.0.CO;2.

Martin, T., M. Steele, and J. Zhang, 2014: Seasonality and long-term trend of Arctic Ocean surface stress in a model. *J. Geophys. Res. Oceans*, **119**, 1723–1738, doi:10.1002/2013JC009425.

McPhee, M. G., 2012: Intensification of geostrophic currents in the Canada Basin, Arctic Ocean. *J. Climate*, **26**, 3130–3138, doi:10.1175/JCLI-D-12-00289.1.

Meredith, M. P., P. L. Woodworth, C. W. Hughes, and V. Stepanov, 2004: Changes in the ocean transport through Drake Passage during the 1980s and 1990s, forced by changes in the southern annular mode. *Geophys. Res. Lett.*, **31**, L21305, doi:10.1029/2004GL021169.

Munday, D. R., H. L. Johnson, and D. P. Marshall, 2013: Eddy saturation of equilibrated circumpolar currents. *J. Phys. Oceanogr.*, **43**, 507–532, doi:10.1175/JPO-D-12-095.1.

Proshutinsky, A., R. Bourke, and F. McLaughlin, 2002: The role of the Beaufort Gyre in Arctic climate variability: Seasonal to decadal climate scales. *Geophys. Res. Lett.*, **29**, 2100, doi:10.1029/2002GL015847.

——, and Coauthors, 2009: Beaufort Gyre freshwater reservoir: State and variability from observations. *J. Geophys. Res.*, **114**, C00A10, doi:10.1029/2008JC005104.

Rabe, B., and Coauthors, 2014: Arctic Ocean basin liquid freshwater storage trend 1992–2012. *Geophys. Res. Lett.*, **41**, 961–968, doi:10.1002/2013GL058121.

Spall, M. A., 2013: On the circulation of Atlantic Water in the Arctic Ocean. *J. Phys. Oceanogr.*, **43**, 2352–2371, doi:10.1175/JPO-D-13-079.1.

——, 2015: Thermally forced transients in the thermohaline circulation. *J. Phys. Oceanogr.*, **45**, 2820–2835, doi:10.1175/JPO-D-15-0101.1.

——, R. S. Pickart, P. S. Fratantoni, and A. J. Plueddemann, 2008: Western Arctic shelfbreak eddies: Formation and transport. *J. Phys. Oceanogr.*, **38**, 1644–1668, doi:10.1175/2007JPO3829.1.

Stewart, K., and T. Haine, 2013: Wind-driven Arctic freshwater anomalies. *Geophys. Res. Lett.*, **40**, 6196–6201, doi:10.1002/2013GL058247.

Su, Z., A. L. Stewart, and A. F. Thompson, 2014: An idealized model of Weddell Gyre export variability. *J. Phys. Oceanogr.*, **44**, 1671–1688, doi:10.1175/JPO-D-13-0263.1.

Tabor, M., 1989: Linear stability analysis. *Chaos and Integrability in Nonlinear Dynamics: An Introduction*, Wiley, 20–31.

Timmermans, M.-L., J. Toole, A. Proshutinsky, R. Krishfield, and A. Plueddemann, 2008: Eddies in the Canada Basin, Arctic Ocean, observed from ice-tethered profilers. *J. Phys. Oceanogr.*, **38**, 133–145, doi:10.1175/2007JPO3782.1.

——, A. Proshutinsky, R. A. Krishfield, D. K. Perovich, J. A. Richter-Menge, T. P. Stanton, and J. M. Toole, 2011: Surface freshening in the Arctic Ocean's Eurasian Basin: An apparent consequence of recent change in the wind-driven circulation. *J. Geophys. Res.*, **116**, C00D03, doi:10.1029/2011JC006975.

——, and Coauthors, 2014: Mechanisms of pacific summer water variability in the Arctic's central Canada Basin. *J. Geophys. Res. Oceans*, **119**, 7523–7548, doi:10.1002/2014JC010273.

Vallis, G. K., 2006: The transformed Eulerian mean. *Atmospheric and Oceanic Fluid Dynamics*: *Fundamentals* and *Large-Scale Circulation*, Cambridge University Press, 304–313.

Visbeck, M., J. Marshall, T. Haine, and M. Spall, 1997: Specification of eddy transfer coefficients in coarse-resolution ocean circulation models. *J. Phys. Oceanogr.*, **27**, 381–402, doi:10.1175/1520-0485(1997)027<0381:SOETCI>2.0.CO;2.

Watanabe, E., 2011: Beaufort shelf break eddies and shelf-basin exchange of Pacific summer water in the western Arctic Ocean detected by satellite and modeling analyses. *J. Geophys. Res.*, **116**, C08034, doi:10.1029/2010JC006259.

——, 2013: Linkages among halocline variability, shelf-basin interaction, and wind regimes in the Beaufort Sea demonstrated in pan-Arctic Ocean modeling framework. *Ocean Modell.*, **71**, 43–53, doi:10.1016/j.ocemod.2012.12.010.

Woodgate, R. A., K. Aagaard, J. H. Swift, K. K. Falkner, and W. M. Smethie Jr., 2005: Pacific ventilation of the Arctic Ocean's lower halocline by upwelling and diapycnal mixing over the continental margin. *Geophys. Res. Lett.*, **32**, L18609, doi:10.1029/2005GL023999.

Yang, J., 2009: Seasonal and interannual variability of downwelling in the Beaufort Sea. *J. Geophys. Res.*, **114**, C00A14, doi:10.1029/2008JC005084.

——, A. Proshutinsky, and X. Lin, 2016: Dynamics of an idealized Beaufort Gyre: 1. The effect of a small beta and lack of western boundaries. *J. Geophys. Res. Oceans*, **121**, 1249–1261, doi:10.1002/2015JC011296.

Zhao, M., M.-L. Timmermans, S. Cole, R. Krishfield, A. Proshutinsky, and J. Toole, 2014: Characterizing the eddy field in the Arctic Ocean halocline. *J. Geophys. Res. Oceans*, **119**, 8800–8817, doi:10.1002/2014JC010488.